



# Frequency- and temperature-dependent dielectric features of multi-component electronic material: $(\text{Pb}_{0.8}\text{Dy}_{0.1}\text{Bi}_{0.1})(\text{Fe}_{0.2}\text{Ti}_{0.8})\text{O}_3$

Satish K. Samal<sup>1</sup> · Sarbasri Halder<sup>1</sup> · Manas Kumar Mallick<sup>1</sup> · R. N. P. Choudhary<sup>1</sup> · Satyanarayan Bhuyan<sup>1</sup>

Received: 11 January 2020 / Accepted: 13 April 2020 / Published online: 29 April 2020  
© Springer-Verlag GmbH Germany, part of Springer Nature 2020

## Abstract

A multiple cation containing sample as  $[(\text{Pb}_{0.8}\text{Dy}_{0.1}\text{Bi}_{0.1})(\text{Fe}_{0.2}\text{Ti}_{0.8})\text{O}_3]$  is fabricated by adopting the solid-state reaction process. The crystallographic structure, crystallite size, morphology, dielectric behavior, conductivity, polarization, impedance as well as electric modulus spectroscopy are experimentally observed for this fabricated composition. The crystal structure of the specimen is observed to be tetragonal from X-ray diffraction. The micrograph shows the presence of polycrystalline microstructure with uniform distributed grains. The impedance spectroscopy analysis as a function of temperature (100–450 °C) and frequency (1–1000 kHz) helps to signify the resistive and capacitive behavior of the compound. The nature of the prepared specimen and conduction mechanism is illustrated through AC conductivity study. The modulus analysis elucidates the existence of non-Debye dielectric relaxation nature in the synthesized compound. The compound possesses appreciable value of loss tangent and remnant polarization, i.e., 0.02 and 0.014  $\mu\text{C}/\text{cm}^2$ , with high value of dielectric constant at room temperature. The dysprosium doping entails stability with interesting electrical and dielectric properties. The preliminary capacitive characteristic has been elucidated, thus making it a stronger contender for functional device applications.

**Keywords** Dy-doped BFO-PT · Dielectric feature · Electronic material

## 1 Introduction

There has been remarkable rising attention for fabricating dielectric ceramics on perovskite system since they can be widely used in various applications such as capacitors, sensor, ultrasonic transducers, computer memories and actuators [1–4]. Generally, lead-based ceramics are preferred due to their enhanced device characteristics although they impose hazardous impact on both health and environment. But nowadays researchers are more focused on developing lead-reduced dielectric materials [5–7]. Bismuth can be an alternative and promising candidate for the substitute of lead [8]. The bismuth-based compound can be special due to their static behavior toward electrodes, lower firing and sintering temperature (i.e., 800–950 °C) [9, 10]. There are various bismuth-based compounds and composites like Bi (Ga, Sc) $\text{O}_3$ –PbTiO<sub>3</sub>, BiScO<sub>3</sub>–PbTiO<sub>3</sub>, BiFeO<sub>3</sub>, etc., which

have been reported with excellent properties equivalent to lead-based compounds, like Pb(ZrTi)O<sub>3</sub>. Among all the bismuth-based compounds, BiFeO<sub>3</sub>(BFO) is found more interesting because of its simpler perovskite structure with the presence of both antiferromagnetic ( $T_N = 643$  K) and ferroelectric ( $T_c = 1143$  K) ordering above room temperature. These properties of the material make it exclusive for multifunctional device applications [11, 12]. Unfortunately, the BFO compound suffers from instinctive problems such as higher loss tangent, lower electrical resistivity, higher coercive field, higher leakage current as well as lack of structural distortion. It may hamper its exclusive properties (resistive, dielectric and ferroelectric). In BFO compound, the higher leakage current occurs due to the oxidation–reduction of Fe ions ( $\text{Fe}^{2+}/\text{Fe}^{3+} + e^-$ ) [13–15]. From the literature survey, it is inferred that by substituting various rare earth or other ions ( $\text{Sm}^{3+}$ ,  $\text{Gd}^{3+}$ ,  $\text{Nd}^{3+}$ ,  $\text{La}^{3+}$ ) at the bismuth site and  $\text{Co}^{3+}$ ,  $\text{Mn}^{4+}$ ,  $\text{Nb}^{5+}$ ,  $\text{Ti}^{4+}$  at the Fe, some defects of BFO can be reduced or minimized to improve the device properties [16–19]. Thus, the attention has been given to multi-component solid solution of BiFeO<sub>3</sub>–PbTiO<sub>3</sub> through chemical modifications by the substitution method in order to enrich the dielectric

✉ Satyanarayan Bhuyan  
satyanarayanbhuyan@soa.ac.in

<sup>1</sup> Department of Electronics and Communication Engineering, ITER, Siksha ‘O’ Anusandhan (Deemed to be University), Bhubaneswar 751030, India

characteristics. The material properties may be enriched by substitution of bismuth ( $\text{Bi}^{3+}$ ) in the place of lead ( $\text{Pb}^{2+}$ ), whereas the substitution of  $\text{Fe}^{3+}$  in  $\text{Ti}^{4+}$  entails its stability [20, 21]. Though significant work has been done on rare earth-doped BFO-PT multi-component system, there is still dearth in the formulation of a new material with the substitution of magnetic rare earth ion (Dy) in BFO-PT with its complete studied electrical and dielectric properties. Hence, in the present research work, it has been tried to solve the problems of BFO and lead titanate simultaneously by fabricating a new stable perovskite electronic system  $[(\text{Pb}_{0.8}\text{Dy}_{0.1}\text{Bi}_{0.1})(\text{Fe}_{0.2}\text{Ti}_{0.8})\text{O}_3]$  by combining both lead titanate and bismuth ferrite and introducing rare earth ion (Dy) as a substituent in the ceramic. The newly prepared compound exhibits interesting structural as well as surface morphological characteristics including electrical and dielectric properties.

## 2 Experimental procedure

The compound  $(\text{Pb}_{0.8}\text{Dy}_{0.1}\text{Bi}_{0.1})(\text{Fe}_{0.2}\text{Ti}_{0.8})\text{O}_3$  has been fabricated by commercial solid-state method using highly pure (> 99.5%) oxide powders of lead titanate, bismuth oxide, ferrous oxide and dysprosium oxide procured from M/S LOBA Chemical, India. The Dy-modified electronic system has been selected after the optimizing synthesis process through balancing the chemical equation in accordance with the charge neutrality condition as given as follows:

$(\text{Pb}_{1-2x}\text{Dy}_x\text{Bi}_x)(\text{Fe}_{2x}\text{Ti}_{1-2x})\text{O}_3 = (1-2x)\text{PbO} + (x/2)\text{Dy}_2\text{O}_3 + (1-2x)\text{TiO}_2 + x\text{Fe}_2\text{O}_3 + (x/2)\text{Bi}_2\text{O}_3$ . The raw elements are weighted by balance (Mettler Type: New Classic MF; Model: ML204/A01) and then they are mixed in dry and wet grinding using a mortar and pestle. The homogeneous mixtures are then calcined in a furnace at a high temperature of 1100 °C for 8 h. The XRD data obtained from X-ray diffractometer are analyzed to check the structure and phase purity of the compound. The software program (POWD) is used to calculate the structural property of the compound and to index the prominent peaks of the diffraction spectrum. The powders after calcination have been mixed with a binder polyvinyl alcohol and pressed to form a disk shape (pellet) by using hydraulic press. The synthesized pellets are then sintered in a furnace at a high temperature of 1200 °C for duration of 8 h. The pellets are then fired with silver paste, and their different electrical behavior (conductivity, dielectric, impedance, modulus) is characterized using LCR meter (model PSM 1735, N4L) at a selected temperature (25 °C–400 °C) and frequency (1 kHz–1 MHz). In the experimental setup along with the LCR meter, a laboratory-fabricated furnace and sample holder are used where the pellet is placed.

## 3 Observed results and discussion

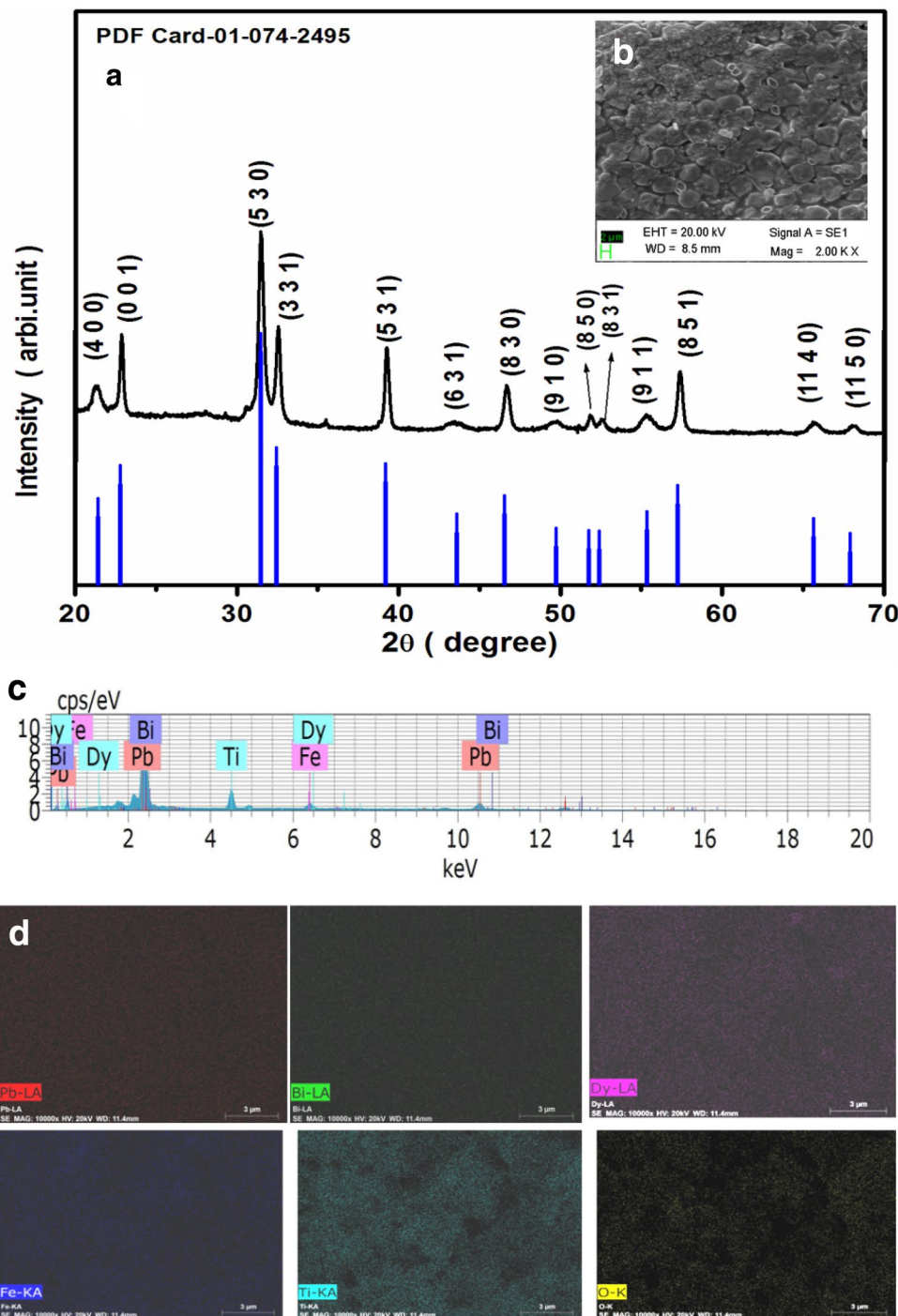
**Structural properties:** To recognize the phase purity as well as the structure of the fabricated compound, X-ray diffraction tool is employed. The experimental XRD spectrum (at room temperature) of ceramic powder of  $(\text{Pb}_{0.8}\text{Dy}_{0.1}\text{Bi}_{0.1})(\text{Fe}_{0.2}\text{Ti}_{0.8})\text{O}_3$  is illustrated in Fig. 1a. As reported in the earlier literature, the system  $(\text{BGxF1-x})\text{-PT}$  showed tetragonal phase [22]. Hence, we refined our XRD data of our fabricated compound in tetragonal crystal symmetry with the help of software package ‘POWD.’ A tetragonal crystal system is chosen on distinguishing a good union between observed and calculated values of  $d$  (inter-planar spacing) of each reflection. The standardized lattice parameters of the selected unit cell are found to be:  $a = 16.609 \text{ \AA}$ ,  $b = 4.1526 \text{ \AA}$ ,  $c = 3.875 \text{ \AA}$ ,  $c/a = 0.2333 \text{ \AA}$  and volume  $V = 1068.63 \text{ \AA}^3$ . (The standard deviation is 0.030.) These unit cell parameters can be normalized to  $a_n = a/4 = 4.1522 \text{ \AA}$ ,  $b = 4.1526 \text{ \AA}$  which is consistent with the tetragonal unit cell of the perovskite. The tetragonal structure of the prepared material is also verified using ‘X’Pert high score’ by comparing it with JCPDS data (PDF card-01-074-2495). The crystallite size ( $S$ ) of the material is analyzed from the X-ray reflection broadening peaks using Scherrer equation  $[P_{hkl}] = \frac{Kk}{\beta_{1/2} \cos \theta_{hkl}}$  where  $K = \text{constant} = 0.89$  and  $k = 1.5405 \text{ \AA}$ ,  $\beta_{1/2}$  (peak width at half-height) and position ( $2\theta$ ) and it is found to be 34 nm.

Figure 1b displays the scanning electron microstructure (SEM) of the sintered pellet (BFO-PT). The micrograph shows the presence of polycrystalline microstructure that can be recognized due to the several randomly uniform distributed grains with small voids on the sample surface.

The availability of different elements (Pb, Bi, Dy, Fe, Ti and O) in the fabricated specimen has been identified from the energy-dispersive X-ray (EDX) spectrum, as depicted in Fig. 1c. The purity of the specimen is asserted as there is no trace of other elements other than Pb, Bi, Dy, Fe, Ti and O in the material. The elemental proportion of Bi, Pb, Fe, Dy, Ti and O is listed in Table 1. The distribution and mapping of different elements (Bi, Pb, Fe, Dy, Ti and O) is exhibited in Fig. 1d that provides the information regarding the fabricated materials.

**Dielectric properties:** In Figs. 2a, b and 3a, b, the frequency- and temperature-dependent dielectric parameters and loss tangent characteristics are illustrated. The  $\epsilon_r$  and  $\tan\delta$  both can be seen to decrease with an increase in frequency for BFO-PT that is similar to all other dielectric compounds [23]. It can be seen from Fig. 2a that at 1 kHz the  $\epsilon_r$  is  $78 \times 10^2$  at 450 °C. At lower-frequency range, the  $\epsilon_r$  of the sample is higher due to oxygen vacancies, the piling of interfacial dislocations, grain boundary effect, etc., whereas at higher-frequency range the  $\epsilon_r$  declines that can be

**Fig. 1** **a** XRD pattern and **b** surface morphological image of  $(\text{Pb}_{0.8}\text{Dy}_{0.1}\text{Bi}_{0.1})(\text{Fe}_{0.2}\text{Ti}_{0.8})\text{O}_3$ . **c** EDX spectrum and **d** mapping image of  $(\text{Pb}_{0.8}\text{Dy}_{0.1}\text{Bi}_{0.1})(\text{Fe}_{0.2}\text{Ti}_{0.8})\text{O}_3$



**Table 1** The elemental proportion of Bi, Pb, Fe, Dy, Ti and O

Element	wt%	at.%
Pb	57.90	21.14
Bi	13.58	4.92
O	10.95	51.77
Ti	9.90	15.64
Gd	4.44	2.14
Fe	3.24	4.39
Total	100	100

caused by accumulation of electrons due to the space charge polarization. The observed trend of an increase in dielectric constant parameter with temperature may be due to the progress of space charges formed during the sintering (volatile nature of bismuth) [24, 25]. Similar characteristics have been noticed for the frequency characteristic of loss tangent. At high temperature, peaks can be observed owing to relaxation phenomenon arising from compositional disorderness [26, 27]. Figure 3c shows the focused low-temperature

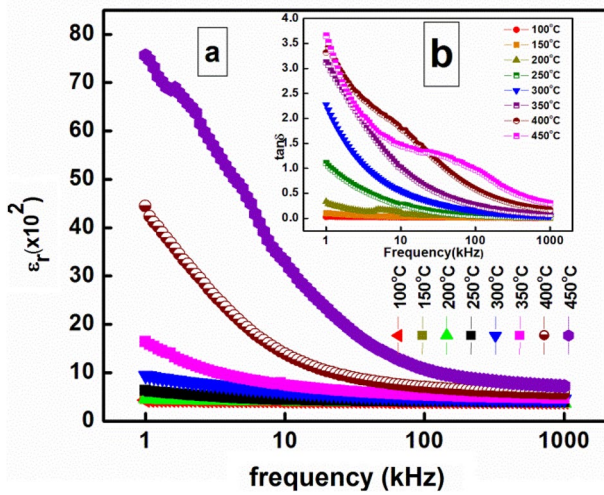


**Fig. 2** a, b Frequency dependence of dielectric constant and loss tangent of the prepared sample

region (> 210 °C) of both dielectric constant and loss tangent of  $(\text{Pb}_{0.8}\text{Dy}_{0.1}\text{Bi}_{0.1})(\text{Fe}_{0.2}\text{Ti}_{0.8})\text{O}_3$ . The plot depicts that the synthesized compound has a higher dielectric constant  $\epsilon_r \sim 400$  at (100 kHz, 25° C) than similar type of compound such as  $(\text{BG}_{0.1}\text{F}_{0.9})\text{-PT}$  that has  $\epsilon_r \sim 150$  and La-modified BFO-PT that has  $\epsilon_r \sim 310$ . It also has a low loss  $\tan \delta \sim 0.06$  at (100 kHz, 25° C) like similar type of compound such as  $(\text{BG}_{0.1}\text{F}_{0.9})\text{-PT}$  that has  $\epsilon_r \sim 0.04$  and La-modified BFO-PT that has  $\epsilon_r \sim 310$  and  $\tan \delta \sim 0.1$  [22, 28].

**Impedance characteristics:** To identify the conduction phenomenon and the influence of grain, grain boundary and electrode in the prepared sample, CIS (complex impedance spectroscopy) has been carried out. Figure 4a, b shows the frequency characteristics of complex impedance ( $Z^*$ ) spectra

(real ( $Z'$ ) and imaginary ( $Z''$ )) part of  $(\text{Pb}_{0.8}\text{Dy}_{0.1}\text{Bi}_{0.1})(\text{Fe}_{0.2}\text{Ti}_{0.8})\text{O}_3$  at different temperatures. The frequency-dependent electrical parameters of the compound are exhibited in terms of admittance, impedance, modulus and loss, and they are linked with each other. The real and imaginary parts of impedance are calculated as follows:

$$\text{Complex permittivity: } \epsilon^* = \epsilon' - j\epsilon''$$

$$\text{Loss tangent: } \tan \delta = \frac{\epsilon''}{\epsilon'} = -\frac{z'}{z''} = \frac{M''}{M'}$$

$$\text{Impedance : } z^* = z' - z'' = R_s \frac{j}{\omega C_s}$$

$$\text{Modulus : } \frac{1}{\epsilon^*} = M^* = M' + jM'' = j\omega C_0 Z^* * \omega$$

$$M' = -\omega C_0 Z \text{ and } M'' = \omega C_0 Z'$$

The  $Z'$  and  $Z''$  of complex impedance are given by the equation given as follows:

$$Z' = \frac{R}{1 + (\omega\tau)^2} \text{ and } Z'' = \frac{\omega R\tau}{1 + (\omega\tau)^2}$$

It can be noticed in Fig. 4a that with the increase in temperature the  $Z'$  declines which signifies an enhancement in the conductivity [29]. The declining nature of  $Z'$  in the low-frequency zone depicts the negative temperature coefficient of resistance (NTCR) nature of the specimen. For different temperatures at high-frequency range, the values of  $Z'$  merge that may happen due to the release of space charges [23].

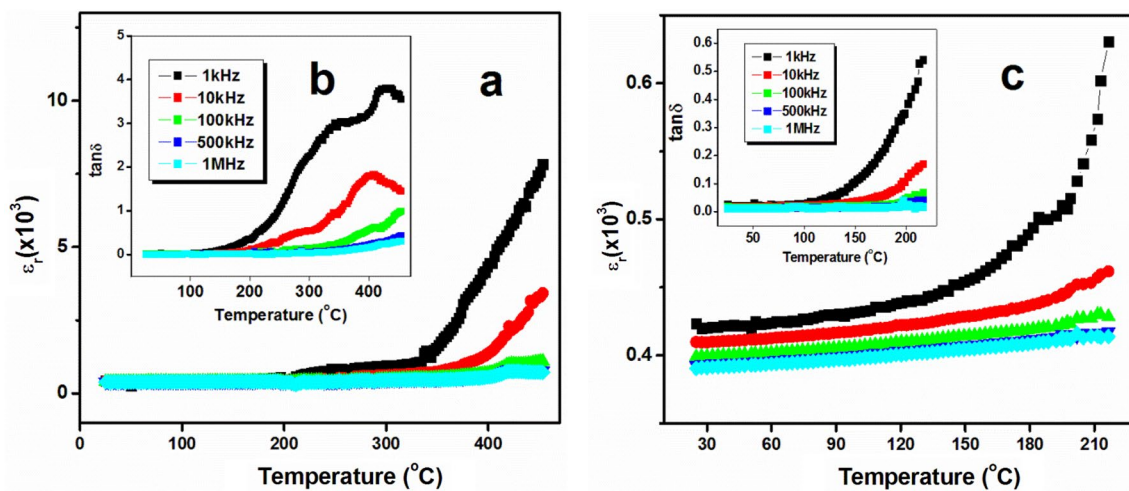


**Fig. 3** a, b Temperature dependence of dielectric constant and loss tangent and c shows the focused low-temperature region (< 230 °C) of dielectric constant and loss tangent of  $(\text{Pb}_{0.8}\text{Dy}_{0.1}\text{Bi}_{0.1})(\text{Fe}_{0.2}\text{Ti}_{0.8})\text{O}_3$

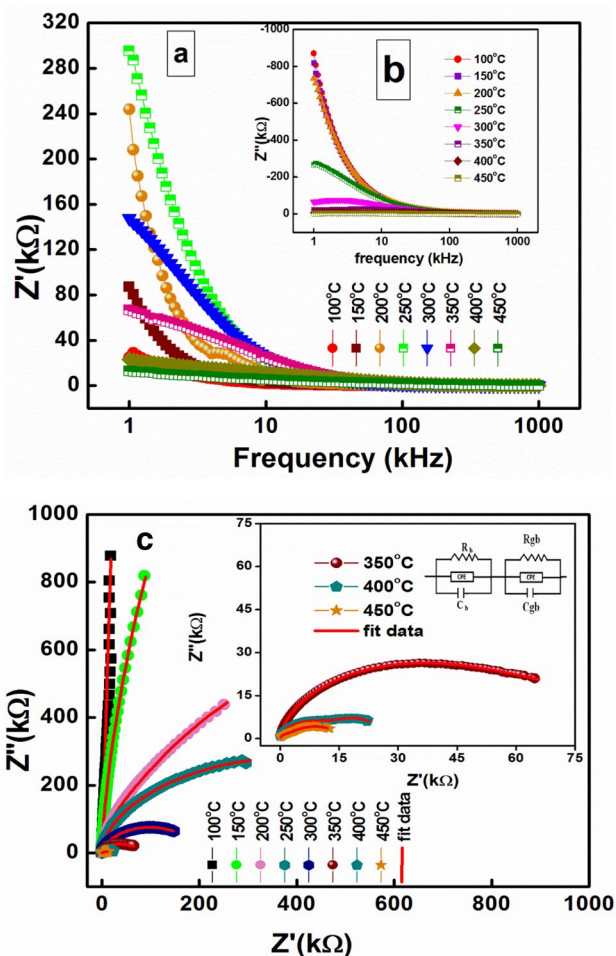


**Fig. 4** Frequency-dependent **a** real and **b** imaginary part of complex impedance of  $(\text{Pb}_{0.8}\text{Dy}_{0.1}\text{Bi}_{0.1})(\text{Fe}_{0.2}\text{Ti}_{0.8})\text{O}_3$ . **c** Nyquist diagram of  $(\text{Pb}_{0.8}\text{Dy}_{0.1}\text{Bi}_{0.1})(\text{Fe}_{0.2}\text{Ti}_{0.8})\text{O}_3$  at different temperatures

The frequency-dependent relaxation behavior arises in the compound due to the vacancy and static charges.

The frequency-dependent  $Z''$  plot is depicted in Fig. 4b which shows that the peaks of  $Z''$  broaden and shift to the high-frequency range with the rise in temperature and merge there. The reason behind this trend may be due to the

accumulation of charge carriers [16]. In the low-temperature zone, the absence of peaks for all samples implies the shortage of current dissipation in the particular temperature range. At a particular frequency, the spectrum shows peaks, which illustrates the strength and type of relaxation mechanism in the compound. The  $Z''$  reaches its max value, and then it moves to the higher frequency zone with a rise in temperature signifying a rise of loss tangent in the compound. The broadening of peaks with the rise in the temperature indicates the presence of relaxation mechanism in the prepared compound [30]. With the increase in temperature, the existence of relaxation times can be indicated by observing the asymmetrical broadening of peaks.

**Nyquist plot:** The obtained Nyquist diagram (analyzed using ZSimpWin software: version 2.0) is illustrated in Fig. 4c. The twist of the impedance curve to form semicircular arcs unveils non-Debye type of relaxation behavior in the compound. A single semicircle is noticed up to the temperature 50 °C that indicates the grains that dominate for the electrical process, whereas the two semicircles observed above 50 °C indicate the result of both grain and grain boundary in the compound. For modeling the semicircular arcs, an electrical equivalent circuit is suggested in accordance with the measured data. The single semicircular arc fit is carried out by  $R_g-Q-C_g$  network, whereas the two semicircular arcs are fitted by  $(R_g-Q-C_g)-(R_{gb}-C_{gb})$  circuit. To affirm the accuracy of the suggested electrical equivalent model, the measured data are fitted with the modeled data. Table 2 shows the grain boundary resistance ( $R_{gb}$ ), grain resistance ( $R_g$ ), grain boundary capacitance ( $C_{gb}$ ), grain capacitance ( $C_g$ ) and constant phase element ( $Q$ ) values measured from the fitted curves.

**Conductive properties:** The inverse temperature-based AC conductivity characteristics of  $(\text{Pb}_{0.8}\text{Dy}_{0.1}\text{Bi}_{0.1})(\text{Fe}_{0.2}\text{Ti}_{0.8})\text{O}_3$  for selected frequencies are displayed in Fig. 5. The electrical conductivity is calculated by using the dielectric data obtained from the LCR meter as follows:

$$\sigma_{ac} = \omega \epsilon_r \epsilon_0 \tan \delta \tag{1}$$

**Table 2** Fitting parameters values of bulk resistance ( $R_g(\Omega)$ ), grain boundary resistance ( $R_{gb}(\Omega)$ ) as well as capacitance of bulk  $C_g(F)$  and grain boundary ( $C_{gb}(F)$ ) at different temperatures

Temperature (°C)	$R_g(\Omega)$	$C_g(F)$	CPE	$R_{gb}(\Omega)$	$C_{gb}(F)$
100	1.284E+003	1.505E-012	7.258E-009	6.403E+007	1.106E-010
150	1.892E+004	2.005E-009	9.554E-008	6.687E+007	1.118E-010
200	3.417E+003	1.082E-009	1.564E-008	3.197E+007	1.157E-010
250	8.619E+004	2.000E-010	5.465E-009	1.519E+007	1.258E-010
300	1.277E+006	2.533E-010	7.405E-009	4.576E+006	1.843E-010
350	7.259E+005	1.100E-010	4.728E-010	3.734E+003	1.840E-010
400	7.579E+004	1.058E-010	1.387E-008	3.275E+002	9.704E-008
450	2.085E+004	1.499E-010	1.205E-007	5.070E+003	3.796E-010

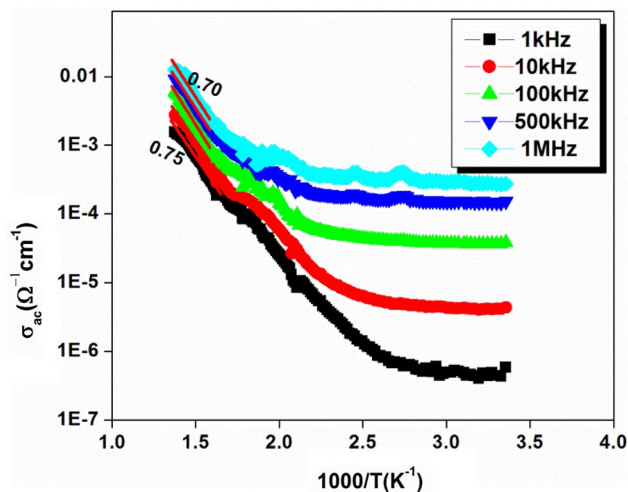


**Fig. 5** AC conductivity plot at selected frequency and temperature of  $(\text{Pb}_{0.8}\text{Dy}_{0.1}\text{Bi}_{0.1})(\text{Fe}_{0.2}\text{Ti}_{0.8})\text{O}_3$

where relative dielectric constant is given by  $\epsilon_r$ , permittivity of free space is  $\epsilon_0$ ,  $\tan\delta$  is the loss and the angular frequency is  $\omega$ .

The plot shows that the conductivity increases with the increase in frequency that indicates the dispersion of conductivity. It can also be noticed that the conductivity curves unite at higher-temperature zone which shows an insight of narrowing of dispersion with a rise in temperature [31]. The temperature characteristic of AC conductivity helps to determine the activation energy by using the Arrhenius equation:

$$\sigma_{dc} = \sigma_0 \exp(-E_a/k_B T) \tag{2}$$

where  $\sigma_0$  is a pre-exponential factor,  $E_a$  is the activation energy and the Boltzmann constant is  $k_B$ . The  $E_a$  is calculated using the fitting data of  $\sigma_{ac}$  versus temperature. For every frequency at different temperature zones, different slopes can be seen in the graph, which suggests the existence of multiple conduction process with varying activation energies in the prepared compound [32, 33].

**Polarization and leakage current study:** Figure 6a displays the room temperature polarization ( $P$ ) versus electric field ( $E$ ) ( $P - E$ ) hysteresis loop. The observed value of the coercive field and remnant polarization of the specimen is 2.30 EV/cm and 0.014  $\mu\text{C}/\text{cm}^2$ , respectively. The voltage ( $V$ ) versus current density ( $J$ ) plot of the sample at room temperature is shown in Fig. 6b. The fabricated pellet shows a lower leakage current density of  $1.72 \times 10^{-9}$  A/cm<sup>2</sup>. The low value of leakage current makes it a suitable candidate for different higher-temperature applications. It can be noticed that the plot is not linear (i.e., rise in current density with the increase in electric field), suggesting the presence of non-Ohmic characteristics in the system.

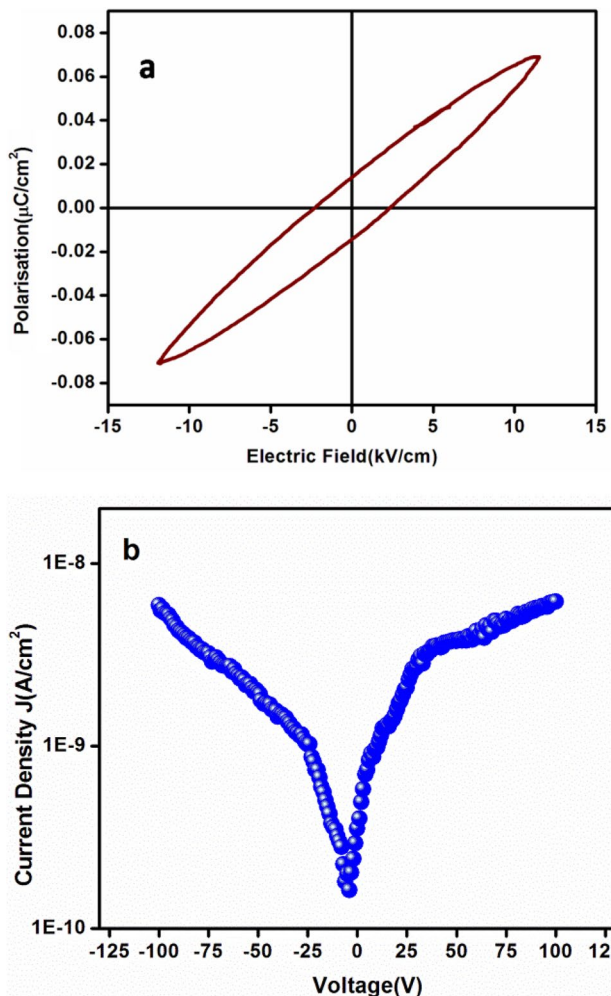


**Fig. 6 a** PE loop **b** leakage current density of  $(\text{Pb}_{0.8}\text{Dy}_{0.1}\text{Bi}_{0.1})(\text{Fe}_{0.2}\text{Ti}_{0.8})\text{O}_3$

**Modulus spectroscopy:** The complex modulus spectrum is a helpful method to analyze the effect of grain and grain boundary, polarization and relaxation phenomena in the sample. The frequency characteristics of modulus (real ( $M'$ ) and imaginary ( $M''$ )) of the electronic material  $(\text{Pb}_{0.8}\text{Dy}_{0.1}\text{Bi}_{0.1})(\text{Fe}_{0.2}\text{Ti}_{0.8})\text{O}_3$  at various temperature are shown in Fig. 7a, b. The  $M'$  and  $M''$  modulus spectrum can be calculated as follows:

$$M' = A \left[ \frac{(\omega RC)^2}{1 + (\omega RC)^2} \right] = A \left[ \frac{\omega^2 \tau^2}{1 + \omega^2 \tau^2} \right]$$

$$M'' = A \left[ \frac{(\omega RC)}{1 + (\omega RC)^2} \right] = A \left[ \frac{\omega \tau}{1 + \omega^2 \tau^2} \right]$$

where  $A = \frac{C_0}{C}$ .

The value of  $M'$  declines at high temperature, and toward the range of lower frequency it approaches zero, while at higher frequency the  $M'$  attains an asymptotic value. This

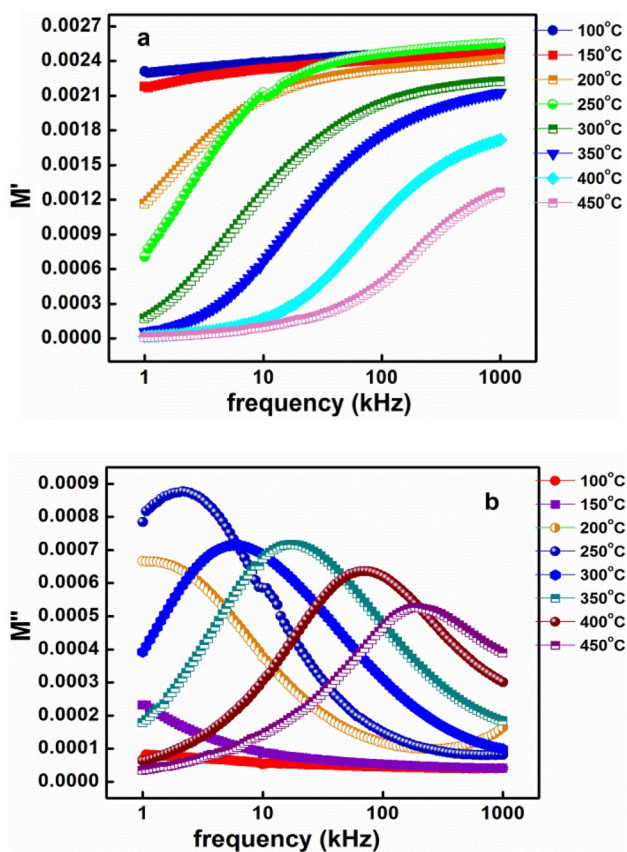


Fig. 7 Frequency-dependent **a** real and **b** imaginary part of complex modulus at different temperatures of  $(\text{Pb}_{0.8}\text{Dy}_{0.1}\text{Bi}_{0.1})(\text{Fe}_{0.2}\text{Ti}_{0.8})\text{O}_3$

type of nature of  $M'$  can be due to the presence of short-range charge carrier and conduction phenomenon. The  $M''$  versus frequency plot (Fig. 7b) shows that the formed peaks of  $M''$  have a tendency to shift toward the range of high frequency. This behavior is more dominating in the higher range of temperature that may be due to the hopping mechanism of charge carriers and its association with relaxation mechanism. The unsymmetrical peak broadening implies the existence of non-Debye of relaxation phenomena with different relaxation time constants [34].

Figure 8 shows the  $M'$  and  $M''$  plot at selected temperature (250–450 °C). It can be seen that for all temperature the asymmetric semicircles tend to overlap with one another that signifies the presence of relaxation mechanism in the sample [35]. The singular arc at the specified temperatures suggests the formation of sample in single phase. The limitations in temperature and frequency withheld the complete formation of curves in lower temperature and frequency.

Figure 9a represents the graph of  $M'$  and  $Z'$  plot which helps to analyze the effect of longer and shorter range movement of charge carriers on the relaxation process. The mismatch of both the peaks ( $M''$  and  $Z''$ ) suggests the role of shorter range charge carriers, whereas the matching of both

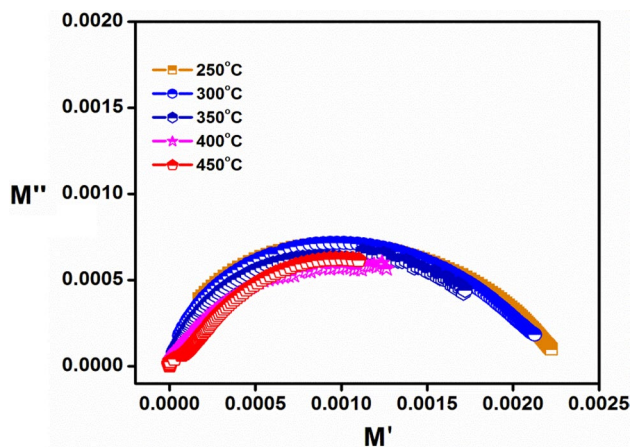


Fig. 8  $M'$  versus  $M''$  plot of  $(\text{Pb}_{0.8}\text{Dy}_{0.1}\text{Bi}_{0.1})(\text{Fe}_{0.2}\text{Ti}_{0.8})\text{O}_3$

peaks at the same frequency symbolizes the presence of longer range motion of charge carriers [36, 37]. As it can be observed from the plot that the peaks ( $M''$  and  $Z''$ ) mismatch

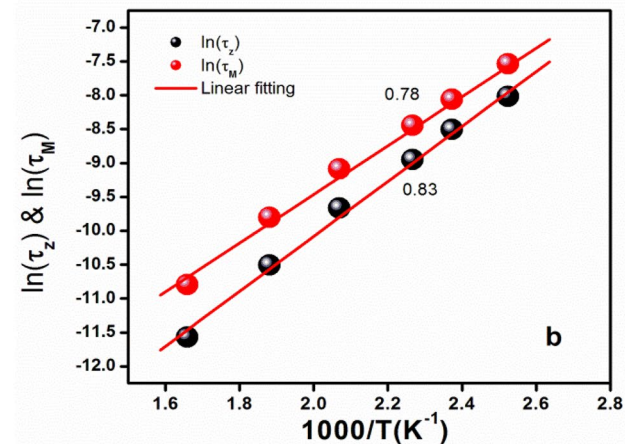
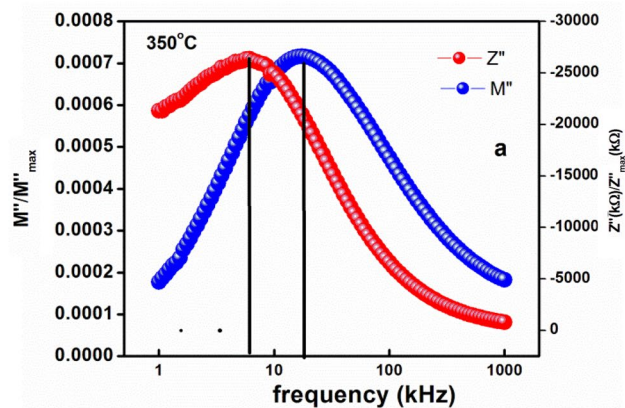
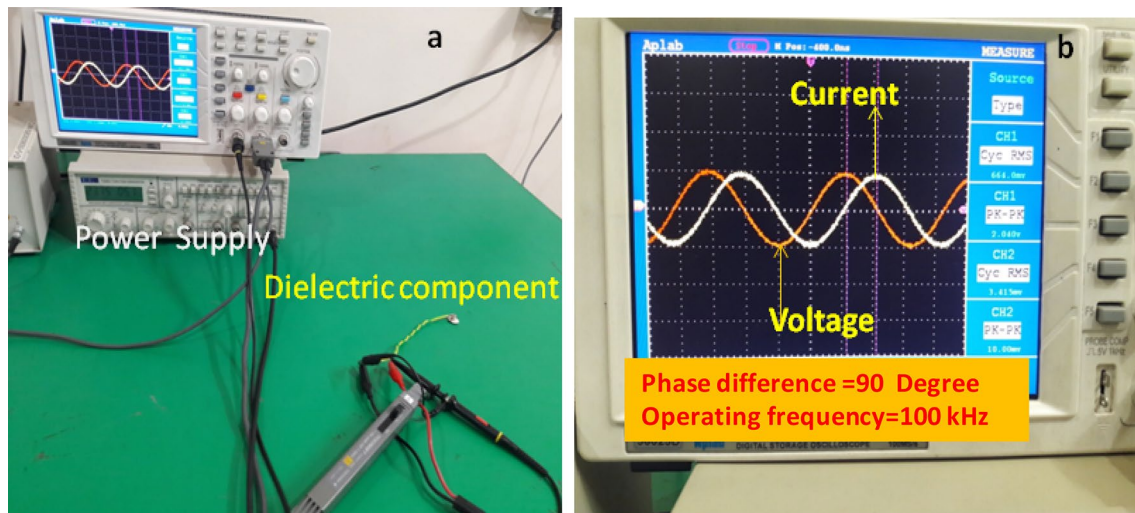


Fig. 9 **a** Frequency-dependent  $M''$  versus  $Z''$  and **b** relaxation time versus inverse temperature plot of  $(\text{Pb}_{0.8}\text{Dy}_{0.1}\text{Bi}_{0.1})(\text{Fe}_{0.2}\text{Ti}_{0.8})\text{O}_3$



**Fig. 10** **a** An experimental setup and **b** capacitive response of the specimen

at a certain frequency, the effect of shorter range movement of charge carrier can be established.

The relaxation time ( $\tau$ ) versus inverse absolute temperature plot is shown in Fig. 9b. It can be seen that both the  $\tau_Z$  and  $\tau_M$  are found to be linear and they obey the Arrhenius equation,  $\tau = \tau_0 \exp(-E_a/K_B T)$ , where  $E_a$  is the activation energy. The  $E_a$  calculated from  $Z''$  is found to be 0.83, that is, nearly equal to the  $E_a$  measured from  $M''$  which is 0.78, signifying that in both the conduction processes the participated charge carriers are equivalent.

#### 4 Preliminary capacitive performance study

To study about the capacitive behavior of the prepared BFO-PT electronic sample, it is excited through electric power supply as depicted in Fig. 10. From the electrical impedance response displayed in Fig. 10b, it can be inferred that the current leads the voltage and a phase difference of  $90^\circ$  at the frequency of 100 kHz which signifies the capacitive nature of the prepared specimen. This preliminary capacitive characteristic has been elucidated, thus making the prepared electronic material a stronger contender for functional device applications.

#### 5 Conclusion

The electronic sample  $(\text{Pb}_{0.8}\text{Dy}_{0.1}\text{Bi}_{0.1})(\text{Fe}_{0.2}\text{Ti}_{0.8})\text{O}_3$  is prepared via solid-state technology at a temperature of 1100. The structural analysis performed on the fabricated compound using XRD data revealed that the specimen has a tetragonal structure at room temperature. The experimental results show that dielectric properties of the Dy-modified

BFO-PT specimen are both frequency and temperature dependent. The conductivity plot of the fabricated sample is seen to obey universal Jonscher's power law. The compound possesses a non-Debye type of relaxation mechanism and NTCR-type behavior that can be confirmed from the impedance characteristics. The presence of a non-exponential-type relaxation phenomenon can be signified from modulus spectrum. The prepared electronic Dy-doped BFO-PT system shows good electrical properties (high dielectric, low loss); hence, it can be used in various technological applications like data storage recorder, random access, transducers, etc.

#### References

1. S. Qing-Xin, P. Kirby, E. Komuro, M. Imura, Q. Zhang, R. Whatmore, *IEEE Trans. Microw. Theory Tech.* **49**, 769 (2001)
2. P. Muralt, M. Kohli, T. Maeder, A. Kholkin, K. Brooks, *Sens. Actuators A* **48**, 87 (1995)
3. H. Chen, M. Jing, Y. Pei, D. Fang, *Int. J. Fract.* **179**, 35 (2013)
4. S. Dutta, A. Pandey, I. Yadav, O.P. Thakur, R. Laishram, R. Pal, R. Chatterjee, *J. Appl. Phys.* **112**, 084101 (2012)
5. Z.G. Lu, G. Calvarin, *Phys. Rev. B.* **51**, 2694 (1995)
6. L.E. Cross, *Ferro* **76**, 241 (1987)
7. N. Settler, L.E. Cross, *J. App. Phys.* **51**, 4356 (1980)
8. C. Soykan, H. Gocmez, *Results Phys.* **13**, 102278 (2019)
9. X. Chen, J. Chen, D. Ma, L. Fang, H. Zhou, *J. Am. Ceram. Soc.* **98**, 804 (2015)
10. C. Zhou, X. Liu, *J. Mater. Sci.* **43**, 1016 (2008)
11. J. Wang, J.B. Neaton, H. Zheng, V. Nagarajan, S.B. Ogale, B. Liu, D. Viehland, V. Vaithyanathan, D.G. Schlom, U.V. Waghmare, N.A. Spaldin, K.M. Rabe, M. Wuttig, R. Ramesh, *Science* **299**, 1719 (2003)
12. N.A. Spaldin, M. Fiebig, *Science* **309**, 391 (2005)
13. S.J. Clark, J. Robertson, *Appl. Phys. Lett.* **90**, 132903 (2007)
14. J. Wei, R. Haumont, R. Jarrier, P. Berthet, B. Dkhil, *Appl. Phys. Lett.* **96**, 102509 (2010)



15. Y.J. Wu, X.K. Chen, J. Zhang, X.J. Chen, *J. Appl. Phys.* **111**, 053927 (2012)
16. V.R. Palkar, J. John, R. Pinto, *Appl. Phys. Lett.* **80**, 1628 (2002)
17. S. Gupta, S. Bhattacharjee, D. Pandey, V. Bansal, S.K. Bhargava, J.L. Peng, A. Garg, *Appl. Phys. A* **104**, 395 (2011)
18. F. Huang, X. Lu, Z. Wang, W. Lin, Y. Kan, H.B. Cai, J. Zhu, *Appl. Phys. A* **97**, 699 (2009)
19. S.H. Baek, H.W. Jang, C.M. Folkman, Y.L. Li, B. Winchester, J.X. Zhang, Q. He, Y.H. Chu, C.T. Nelson, M.S. Rzechowski, X.Q. Pan, R. Ramesh, L.Q. Chen, C.B. Eom, *Nat. Mater.* **9**, 309 (2010)
20. J.G. Chen, Z. Xu, X. Yao, *Mater. Res. Innov.* **14**, 234 (2013)
21. J. Cheng, S.W. Yu, J. Chen, Z. Meng, L.E. Cross, *Appl. Phys. Lett.* **89**, 122911 (2006)
22. E.E. Wu, *J. Appl. Cryst.* **22**, 506 (1989)
23. L. Thorsten, T. Granzow, J. Wook, J. Rödel, *J. Appl. Phys.* **108**, 014103 (2010)
24. A. Reetu, S. Agarwal, N. Sanghi, Ahlawat, Monica, *J. Appl. Phys.* **111**, 113917 (2012)
25. K.K. Mishra, A.T. Satya, A. Bharathi, V. Sivasubramanian, V.R.K. Murthy, A.K. Arora, *J. Appl. Phys.* **10**, 123529 (2011)
26. J.E. Garcia, V. Gomis, R. Perez, A. Albareda, J.A. Eiran, *Appl. Phys. Lett.* **91**, 0429021 (2007)
27. Z. Dai, Y. Akishige, *J. Phys. D Appl. Phys.* **43**, 445403 (2010)
28. S.K. Pradhan, S.N. Das, S. Bhuyan, C. Behera, R. Padhee, R.N.P. Choudhary, *Appl. Phys. A* **122**, 604 (2016)
29. S. Sharma, V. Singh, O. Parkash, R.K. Dwivedi, *Appl. Phys. A* **112**, 975 (2013)
30. B. Behera, P. Nayak, R.N.P. Choudhary, *Mater. Res. Bull.* 43401 (2008)
31. K. Parida, S.K. Dehury, R.N.P. Choudhary, *Phys. Lett. A* **380**, 4083 (2016)
32. P. Gupta, R. Padhee, P.K. Mahapatra, R.N.P. Choudhary, *Mater. Electron.* <https://doi.org/10.1007/s10854> (2017)
33. J.R. Macdonald, *Chapter 4* (Wiley, New York, 1987)
34. S. Chatterjee, P.K. Mahapatra, R.N.P. Choudhary, A.K. Thakur, *Phys. Status Solidi (a)* **201**, 588 (2004)
35. X. Chai, X. Sun, L. Pang, Bismuth Nickel Niobate with Small Negative Temperature Coefficients of Dielectric Constant, *IEEE*, pp. 1–3 (2017)
36. N. Setter, R. Waser, *Electroceram. Mater. Acta Mater.* **48**, 151–178 (2000)
37. N.K. Mohanty, A.K. Behera, S.K. Satpathy, B. Behera, P. Nayak, *Solid State Physics. AIP Conference Proceedings* 15, p. 1330 (2014)

**Publisher's Note** Springer Nature remains neutral with regard to jurisdictional claims in published maps and institutional affiliations.